ORIGINAL PAPER

A Pre-peak Elastoplastic Damage Model of Gosford Sandstone Based on Acoustic Emission and Ultrasonic Wave Measurement

Xu Li[1] · Guangyao Si[1] · Joung Oh[1] · Ismet Canbulat[1] · Zizhuo Xiang[1] · Tianbin Li[2]

Abstract

The determination of internal material damage is always an arduous challenge. Non-destructive monitoring methods show great potential in quantitatively determining the internal material properties, whereas most of the studies relying on external observations remain in a qualitative stage. They either violate the basic thermodynamic assumptions or are difficult to guide engineering practice. In this paper, following the theory of continuum mechanics, an elastoplastic damage model based on non-destructive monitoring methods (i.e., acoustic emission and ultrasonic wave velocity measurement) has been developed. To capture the continuous and precise damage evolution inside rock mass, P wave velocity obtained by ultrasonic wave measurement was utilised and then considered as an input for the proposed elastoplastic damage model. Triaxial loading test results on six Gosford sandstone samples were analysed first to characterise critical stresses along the stress–strain loading curves, such as crack closure stress, stable crack propagation stress and unstable crack propagation stress. The drop of ultrasonic wave velocity can be seen as an indicator to represent the damage evolution inside rock material. Damage initiation is also closely related to the confining stress and dilation induced volumetric expansion. The test results also suggested that the Drucker–Prager criterion is sufficient to describe the plastic yielding surface and the following material hardening. A non-associated plastic flow assumption was adopted, considering the essence of microcrack shearing in rock failure and the effect of hydrostatic pressure on plastic deformation. A modified Drucker–Prager plastic potential was also introduced to track the orientation of plastic increment with material hardening. A scalar damage variable was derived from ultrasonic wave measurement results to indirectly represent the deterioration of rock properties (modulus). The proposed model was used to match lab test results with high consistency, and the main features of rock behaviour in triaxial loading tests were successfully captured by the model. Finally, the damage evolution of rock samples was analysed, which indicates that damage is dependent on its conjugate force, namely damage energy release rate Y. This study proves that P wave velocity can be an effective approach to measure and forecast the internal damage evolution inside rock mass, which has broad prospects for engineering applications.

Highlights

- An elastoplastic damage model with non-associated plastic flow and scalar damage variable has been developed.
- P wave velocity is found to be closely related to the expansion of volumetric strain and damage evolution.

✉ Guangyao Si
g.si@unsw.edu.au

✉ Tianbin Li
ltb@cdut.edu.cn

1   School of Minerals and Energy Resources Engineering, University of New South Wales, Sydney, NSW 2052, Australia

2   State Key Laboratory of Geohazard Prevention and Geoenvironment Protection, Chengdu University of Technology, Chengdu 610059, China

List of Symbols

$\tilde{A}$	Effective cross-sectional area
A	Total cross-sectional area
A_ω	Void cross-sectional area
σ_c	Crack closure stress
σ_{ci}	Crack initiation stress
σ_{cd}	Crack damage (coalescence) stress
σ_f	Peak stress
σ_{ij}	Stress tensor with six independent variables
$\tilde{\sigma}_{ij}$	Effective stress
ε_{ij}	Total strain
ε_{ij}^e	Elastic strain
ε_{ij}^p	Plastic strain
ε_x^p	Principal plastic strain in the x-axial direction
ε_y^p	Principal plastic strain in the y-axial direction
ε_z^p	Principal plastic strain in the z-axial direction
ε_i^p	Cumulative plastic strain
C_{ijkl}^0	Initial (undamaged) stiffness matrix
$C_{ijkl}(\omega)$	Damaged stiffness matrix
V_p	P wave velocity
E	Young's modulus
$\tilde{E}$	Effective Young's modulus
ν	Poisson's ratio
V^k	Direction of kth principal stress
φ	Total Helmholtz free energy
φ_e	Elastic Helmholtz free energy
φ_p	Plastic Helmholtz free energy
φ_ω	Damage Helmholtz free energy
f_p	Plastic yielding surface
g_p	Plastic potential
γ_p	Plastic hardening variable
α_p	Conjugated force according to the plastic hardening variable γ_p
α_1	Parameter for plastic hardening magnitude
β_1	Parameter for plastic initiation
p	Parameter for volumetric plastic strain in modified Drucker–Prager plastic potential
α_2	Parameter for plastic hardening magnitude
β_2	Parameter for plastic initiation
$\Upsilon_2,$	Fitting parameters to determine the acceleration of plastic strain
σ_α	Critical confinement, where volumetric strain is the maximum
λ_p	Plastic multiplier
α	Drucker–Prager parameter
f_ω	Damage yielding surface
g_ω	Damage potential
λ_ω	Damage multiplier
$\tilde{I}_1$	First invariant of effective stress tensor
$\tilde{J}_2$	Second invariant of deviatoric effective stress tensor
$k_{0/f}$	D–P parameter for initial plastic yielding surface (k_0) and final failure surface (k_f)
ω	Scalar damage variable
Y	Damage energy release rate (conjugate force of damage variable)

1 Introduction

Rock plays a significant role in mining, oil and gas, civil and nuclear waste disposal applications. An effective approach to evaluate rock properties is to conduct lab-scale tests. The elastic, plastic and post-peak stages can be easily identified from the stress–strain curves obtained with the assistance of various monitoring approaches, such as acoustic emission (AE), ultrasonic velocity, and computed tomography (CT) (Cai et al. 2004; Kong et al. 2018). However, one of the most salient problems is that the non-linear deformation of rock exhibited is too complicated to be explicated in the pre-peak stage. The pre-peak stage forms considerable microcracking, aggregating the development of rock damage (Zhao 1998; Homand et al. 2000; Ganne et al. 2007), which plays a predominated role in rock failure. In addition, the pre-peak energy evolution, stress state and stress–strain relationship can identify rock brittleness and ductility in its early stage (Munoz et al. 2016; Zhang et al. 2021a, b, c), which directly affect the rock post-peak behaviour and can be used as important indicators for rockburst risk assessment (Cai et al. 2019; Li et al. 2021). Moreover, in geophysics, the pre-peak behaviour of rock shearing is an indicator for earthquake initiation (Fathi et al. 2016; Liu et al. 2018). Hence, understanding the evolution of rock elastoplastic damage in the pre-peak stage is essential in rock engineering.

In the scope of continuum mechanics, the pre-peak non-linear loading behaviour is explained as an extremely complex process, normally a combination of two unmeasurable internal variables, namely plasticity and damage. Plastic deformation is defined as a permanent distortion of rock grains, characterised as irreversible deformation. The plastic flow rule, plastic yielding function, hardening law and plastic potential set the solid foundation of the plasticity theory in rock engineering (Hill 1948; Wilkins 1963). The associated plastic flow rule is widely applied to metal material, where the magnitude and direction of plastic deformation are controlled by the plastic multiplier and gradient of plastic yielding surface, respectively. The effect of hydrostatic pressure is normally ignored in the associated plastic flow, for example, as model assumptions in the von Mises yield criterion. Recent research shows that the associated plastic flow rule can roughly estimate the plasticity of rock specimens (Zhang et al. 2021a). However, as a typical frictional material, the plastic behaviour of rock is related to the slip of microcracks (shear failures), where the increment of plastic strain generally does not coincide with the gradient of plastic yield function (Lockner et al. 1992; Li et al. 2017; Oh et al.

2017). In addition, the confinement (hydrostatic stress) is proved to be an important factor affecting the rock mechanical properties since the component normal to microcracks can constrain shear slippage (Wu et al. 2016; Xu et al. 2018). Therefore, the plastic behaviour of rock should be described by a non-associated plastic flow rule, where the plastic yielding surface and plastic potential function do not coincide with each other (e.g., the volumetric plastic strain cannot be properly estimated via associated plastic flow), and the effect of hydrostatic pressure on plastic deformation needs to be considered as well (Raniecki and Bruhns 1981; Qin and Bassani 1992; Shao et al. 2006).

Apart from plastic deformation, damage is also found to be an essential factor affecting the overall rock behaviour. The damage theory was first introduced in the 1950s (Kachanov 1958, 1986) and fast developed in the early 2000s (Lemaitre et al. 2000; Chiarelli et al. 2003). Rock damage is indicated by the deterioration of rock properties (normally Young's modulus) during compressive loading tests. A damage variable should be defined as a scalar, second-order tensor or even fourth-order tensor to describe the extent of reduction on material properties (Krajcinovic 1996; Murakami and Kamiya 1997).

Numerous elastoplastic damage models were proposed by many pioneering researchers to simulate the non-linear loading behaviour of rock (Salari et al. 2004; Shao et al. 2006; Chen et al. 2010; Shojaei et al. 2014; Balieu and Kringos 2015; Zhang et al. 2016; Cai et al, 2018). These models can be separated into two categories, stochastic and phenomenological models. The stochastic method mainly uses a probability distribution function (e.g., Normal distribution, Poisson distribution, or Exponential distribution) to mimic the distribution of certain rock mass properties (e.g., strength) and, therefore, the overall non-linear loading behaviour (Tang et al. 1997; Li and Chen 2009; Li et al. 2012; Chen et al. 2018; Shen et al. 2019). However, this type of model is less convincing since the true internal heterogeneity of rock samples is hard to be directly verified. On the other hand, the phenomenological method focuses on fitting lab test results with constitutive models. Even though some parameters may not have clear physical meanings, these constitutive models can be easily modified and used for numerical simulation, which provides unparalleled modelling advantages (Zhao et al. 2017).

From the elastoplastic and damage evolution models mentioned above, both damage and plastic (hardening) variables are normally considered as internal variables, which means their direct verification is difficult. Therefore, although the above models can show excellent agreement in fitting experiment curves, the description of internal damage and plasticity evolution may still be unsatisfactory due to the lack of verification. One possible approach to illustrate the plastic and damage evolution prior to rock failure is to conduct a few unloading cycles through the whole compressive loading test to obtain Young's modulus and plastic deformation (Salari et al. 2004; Grassl and Jirásek 2006; Chen et al. 2015). After unloading, the residual deformation represents the plastic strain and the reduction of Young's modulus indicates the induced damage. However, too many unloading cycles can accelerate material fatigue which may affect the following plastic and damage evolution (Attewell and Farmer 1973; Singh 1988; Li et al. 2020a). In addition, the continuous evolution of plastic and damage yet cannot be fully captured with only a limited number of unloading cycles. Continuous measurement of damage evolution is in great demand to assist the understanding of rock non-linear behaviour.

To understand the internal material structural change (damage), non-destructive testing (NDT) methods show great potential and have already been widely adopted in lab-scale rock testing in recent years, e.g., ultrasonic wave velocity measurement (Iyare et al. 2021), acoustic emission (Ishida et al. 2017; Su et al. 2018; Miao et al. 2021), nuclear magnetic resonance (Li et al, 2020b, 2020c) and CT scanning (Xu et al. 2020). These NDT methods can detect microscale rock property change without inducing new damage. Considering the convenience and future prospects in underground engineering applications (Si et al. 2015, 2020; Cao et al., 2020), AE and ultrasonic wave velocity measurements were applied in this research.

In this paper, a new elastoplastic damage evolution model to describe the pre-peak stage of Gosford sandstone under compressive loading has been proposed following the framework of continuum mechanics. With the assistance of two NDT methods (AE and ultrasonic wave velocity), the continuous damage evolution inside rock samples during triaxial compressive loading tests was quantified. The corresponding plastic flow and damage evolution were well simulated by the proposed model. This study also proves that the non-destructive monitoring methods, especially P wave velocity measurement can efficiently detect the internal damage of rock.

2 Laboratory Rock Testing

2.1 Experiment Material and Sample Preparation

The rock material tested here is Gosford sandstone collected from the Gosford Quarry, New South Wales, Australia. Gosford sandstone is widely distributed around the Sydney region and used as civil construction material. The mechanical property of Gosford sandstone was extensively investigated in previous studies (Roshan et al. 2016, 2017; Masoumi et al. 2016; Lv et al. 2019; Keneti et al. 2021). Due to its homogeneity and isotropy, Gosford sandstone can

be regarded as an ideal material for rock testing. The major mineral in Gosford sandstone is 86% quartz, 7% illite, 6% kaolinite and 1% anatase (Roshan et al. 2016; Masoumi et al. 2017), with poorly cemented medium grains (0.2–0.3 mm). The typical porosity of Gosford sandstone is 5% and its density is around 2226.5 kg/m^3 (Ord et al. 1991). In this research, rock samples used in triaxial loading experiments were carefully examined to ensure no pre-existing cracks. The samples were core drilled into cylinders with 50 mm in diameter and 100 mm in height. The ISRM suggested procedure was followed during the preparation of the sandstone samples (Fairhurst, 1997).

2.2 Experiment Setups

Six Gosford sandstone samples were prepared to be tested under triaxial compressive loading. All triaxial tests were conducted under a servo-controlled hydraulic universal testing frame with a loading capacity of 3600 kN (Li et al. 2016a, b), as shown in Fig. 1. The frame enables to select either force-controlled or displacement-controlled loading cycles. In this work, the axial displacement was selected as the feedback signal to control the whole loading process.

The loading cell is the HTRX-140XL rock triaxial cell supplied by Geotechnical Consulting and Testing Systems (GCTS Testing Systems) in the US, with the maximum confining pressure of 140 MPa. The largest sample that can be placed in the loading cell is 76 mm in diameter and 152 mm in height. A pressure intensifier with a maximum capacity of 120 MPa was utilized to provide confining pressure.

The axial and circumferential strain were measured by two Linear Variable Differential Transformers (LVDTs) and their displacement measurement range is 25 mm, which is sufficient to measure the rock deformation in the designed triaxial tests. All the LVDTs were calibrated by the supplier GCTS to ensure the accuracy of displacement measurement.

High-frequency sinusoid ultrasonic waves (1000 kHz) can be motivated from the loading platen for P wave velocity measurement by the GCTS ULT-200 system (input voltage: 12 V), as shown in Fig. 1. Ultrasonic velocity measurement was conducted every five seconds during the test, ensuring continuous monitoring of rock damage development. To reduce the influence of possible voids generated between the loading platen and the rock sample, honey was used as the coupling material between them, as suggested by GCTS.

To detect the internal behaviour of test material, especially the microcrack generation and propagation, AE monitoring was adopted in this study. During the whole loading process, an eight-channel AE data acquisition system provided by MISTRA was also applied to record and process AE data, as shown in Fig. 1. Eight AE sensors (AE-HTRX-50 from GCTS, frequency range: 0–500 kHz) were adhered onto the thermal shrinkage outside the rock sample using hydrothermal glue to collect waveform singles generated by rock failure. The layout of the sensor array can be seen in Fig. 1. The arrival time of AE hits was automatically captured and then Geiger's method was used to back-calculate the location of AE events.
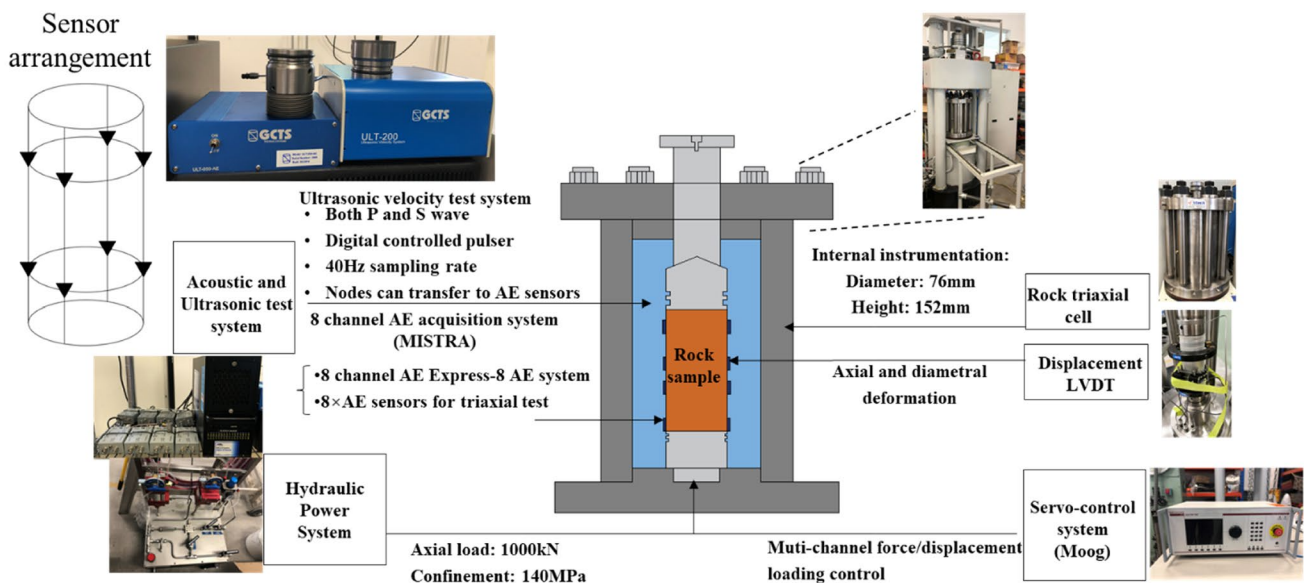

Fig. 1 Lab testing equipment used for triaxial loading with ultrasonic and AE monitoring
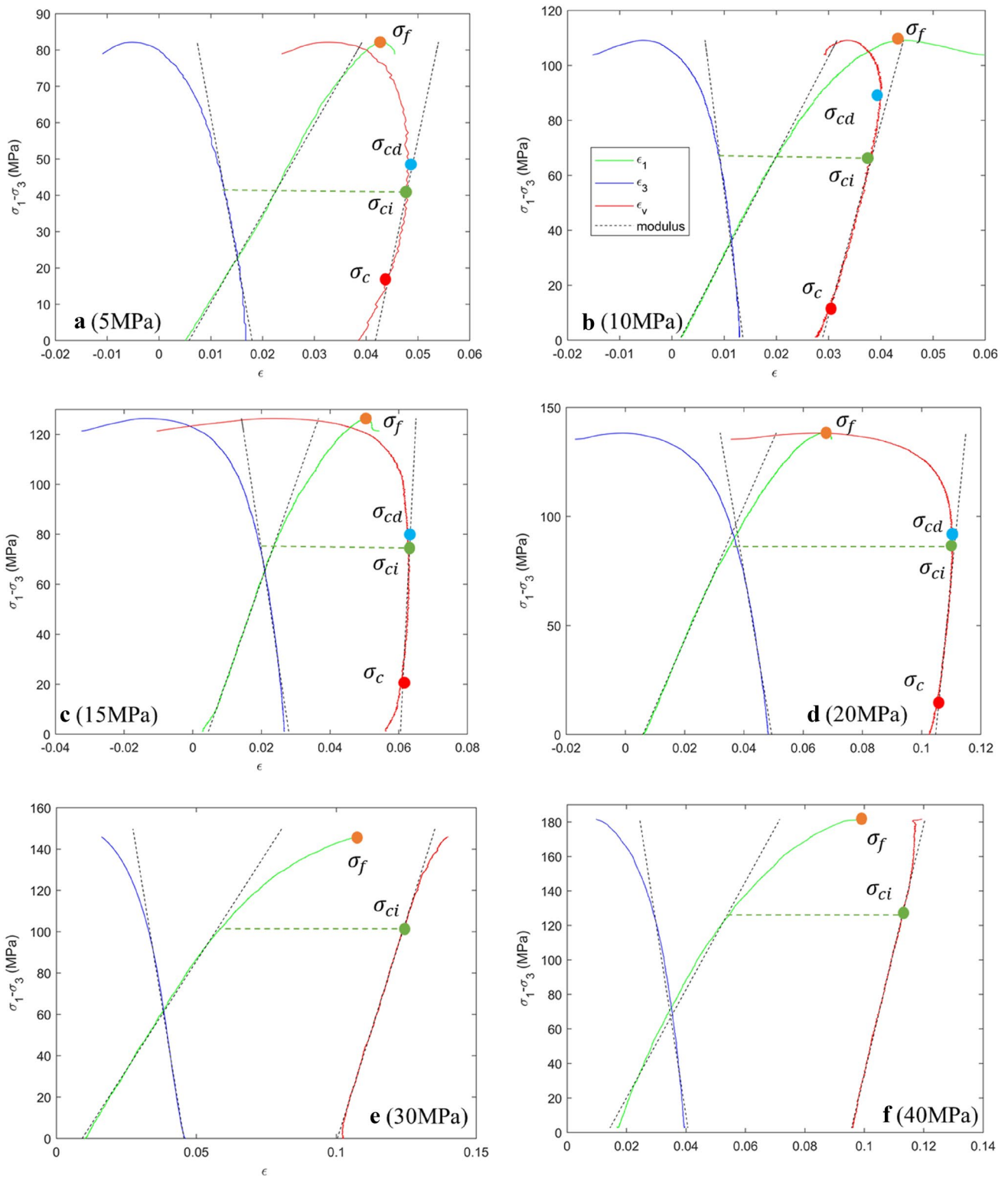
Fig. 2 Stress–strain curves for triaxial tests on Gosford sandstone under a variety of confinements (5 MPa, 10 MPa, 15 MPa, 20 MPa, 30 MPa and 40 MPa). The crack closure stress (σ_c), crack initiation stress (σ_{ci}), crack coalescence stress (σ_{cd}) and peak stress (σ_f) are marked in red, green, blue and yellow dots on these curves

2.3 Test Procedures

In this study, six triaxial tests were conducted with a variety of confining pressure. The confining stresses were set as 5 MPa, 10 MPa, 15 MPa, 20 MPa, 30 MPa and 40 MPa for all six samples. At the beginning of the test, confinement was applied to the rock sample with a constant loading rate at around 0.1 MPa/s. Then the servo-control valve motivated the top platen to add axial load on the rock specimen until the peak stress was reached and stress-softening behaviour was observed.

3 Test Results

3.1 Stress–Strain Curves and Yielding Surface

Figure 2 presents the pre-peak stress–strain curves of six sandstone samples under a variety of confinements (5 MPa, 10 MPa, 15 MPa, 20 MPa, 30 MPa and 40 MPa). ε_1, ε_3, and ε_V indicate axial strain, lateral strain and volumetric strain, respectively. The overall stress–strain curve can be divided into two or three different stages. The 5 MPa, 10 MPa, 15 MPa and 20 MPa scenarios start from the crack closure stage (σ_c), where a concave non-linear stress–strain relation was observed when axial loading was just applied (Zhang and Tang 2020). Then it is followed by the elastic stage, where stress increased linearly with recoverable strain changes. The curves presented here are in the deviatoric stress space meaning that the application of hydrostatic pressure is not included. In the 30 MPa and 40 MPa scenarios, the confinement is high enough to close microcracks before the application of axial load, and hence the crack closure stage is not identified in those two scenarios. By the end of the elastic stage, the stress strain curve (both lateral and volumetric strain) became non-linear again. The stress at this point was defined as the crack initiation stress (σ_{ci}), where the stable crack growth began inside the rock with the presentation of associated unrecoverable plastic strain (Nicksiar and Martin 2012; Zhao et al. 2015). Two methods were applied to identify the crack initiation stress (σ_{ci}). The first method is the lateral strain method, where crack initiation stress (σ_{ci}) is defined as the point, where the lateral stress–strain curve is not linear. The second method is the volumetric strain method, where crack initiation stress (σ_{ci}) is the end of linear correlation between the axial strain and volumetric strain (Brace et al. 1966; Martin and Chandler 1994; Zhao et al. 2015). The crack initiation stress (σ_{ci}) identified by these two methods shows great consistency. After that, the unstable crack growth stress was reached (which is named the crack damage stress, σ_{cd}), and at this point the volumetric strain started to reverse (from compassion to

dilation) (Vásárhelyi and Bobet 2000; Zhang et al. 2021b). This stage was noted as the crack damage stage, which was characterised by a drop in ultrasonic wave velocity, intensified plastic deformation, the boost of AE events, and damage initiation (will be discussed in Sects. 3.2 and 3.3). Then, the final failure occurred when the peak stress was reached (σ_f).

An interesting observation is that the reverse of volumetric strain did not appear in Fig. 2e, f (30 MPa and 40 MPa confinement, respectively). That is due to the fact that the high hydrostatic stress confines the lateral expansion of rock mass prior to reaching the peak stress. The microcracks are compacted by the high confinement and once sliding is initiated, the asperities would be sheared off so that dilation tendency is restricted (Patton 1966). Therefore, the volumetric expansion was not observed in the pre-peak stage for samples under high confinements, which is also illustrated in the previous sandstone loading tests (Bésuelle et al. 2000; Klein et al. 2001).

The crack initiation stress (σ_{ci}) indicates that rock has already entered the plastic stage. In other words, the crack initiation stress is actually on the initial plastic yielding surface. Any additional stress applied beyond that point will lead to irreversible plastic strain. In addition, the yielding surface (also referred to as the loading surface) expands as the increase of material loading until the failure stress is exceeded, namely the material hardening process. The peak (failure) stress (σ_f) is on the failure surface, which is the ultimate yielding surface after which strain-softening replaces hardening. Therefore, the plastic yielding surface is an essential part to control the plastic flow and should be determined carefully. To ensure that the plastic yielding surface is selected properly, the evolution of crack initiation
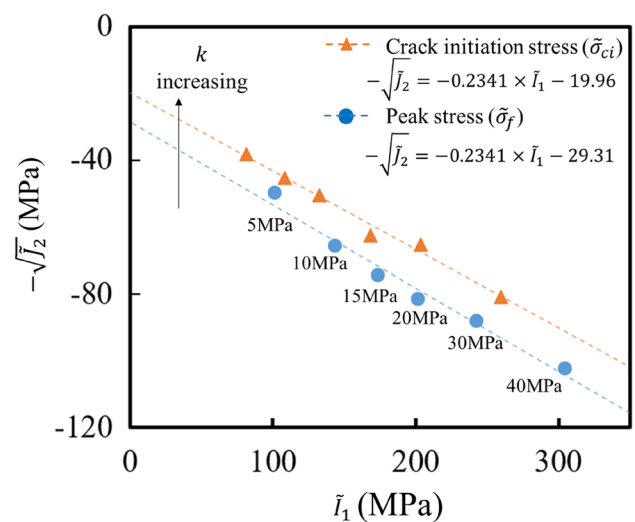

Fig. 3 Cross-plot of crack initiation stress (σ_{ci}) and peak stress (σ_f) (fitted by the Drucker–Prager criterion)

stress (σ_{ci}) and peak stress (σ_f) are shown in Fig. 3, which are represented by the corresponding first and second stress invariant. The Drucker–Prager criterion is proved to be sufficient to describe the yielding surface in this research, as formulated in the following equation:

$$f_p\left(\tilde{\sigma}_{ij}, \gamma_p, \omega\right) = \alpha\tilde{I}_1 + \sqrt{\tilde{J}_2} - k \tag{1}$$

where f_p is the plastic yielding surface, $\tilde{I}_1$ and $\tilde{J}_2$ are the first invariant of the effective stress tensor and second invariant of the deviatoric effective stress tensor. The definition of effective stress will be systematically introduced in Sect. 3.3. α is a factor considering the effect of hydrostatic pressure on the plasticity. k is the D–P parameter to measure plastic hardening, and k_0 and k_f are two constants indicating the hardening degree for the initial plastic yielding surface and final failure surface, respectively. From the test results, we observed that the hydrostatic pressure variable α can be considered as a constant (-0.2341) for the whole plastic evolution range from $\tilde{\sigma}_{ci}$ to $\tilde{\sigma}_f$. k is increasing with the progressive development of plasticity (from $k_0 = 19.96$ to $k_f =37.10$), which can be considered as a factor related to material hardening (expansion of the yielding surface).

3.2 AE Temporal and Spatial Evolution

The location of AE events can provide a direct measurement of the microcrack initiation and propagation inside rock materials. The AE results should be strongly related to the damage and plasticity evolution of rock specimens. Herein, we use the sample with 10 MPa confinement as an example to explain the relationship between AE and non-linear rock deformation. Figure 4 shows the spatial and temporal (in colour) distribution of AE events and their corresponding energy (pseudo energy, which is defined as the integration of signal voltage to time) in different loading stages,
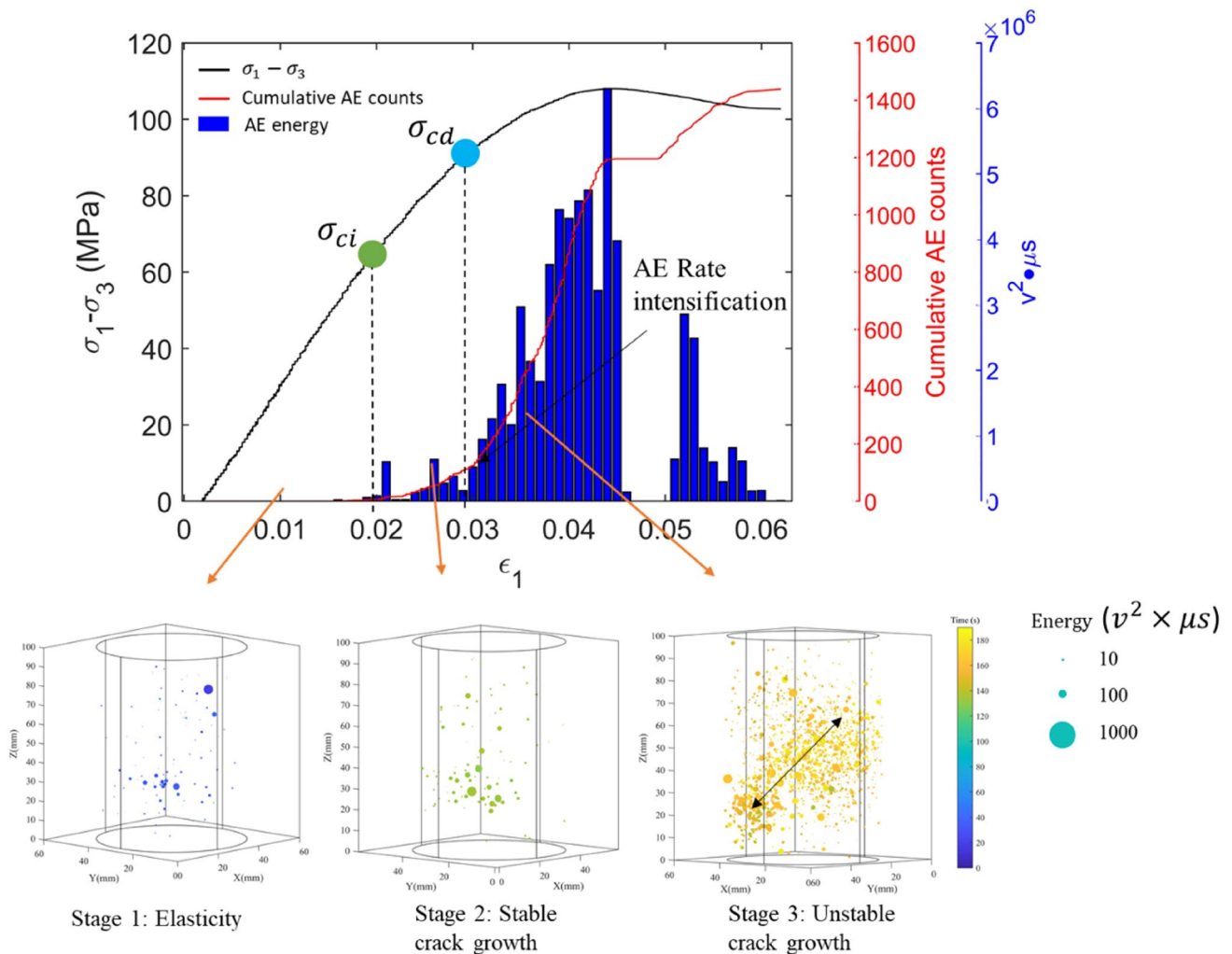

Fig. 4 Cumulative number and energy of AE events and their spatial distribution in the elastic, stable crack growth and unstable crack growth stages (10 MPa confinement)

including the elastic, stable crack growth and unstable crack growth stages. In the elastic stage, only a few AE events were detected, and the corresponding energy of AE events was low (below 200 $v^2 \times$ μs). Once entered the stable crack growth stage (from σ_{ci} to σ_{cd}), although the number of AE events only slightly increased, the energy of AE events was much higher than that in the elastic stage (up to $10^3 v^2 \times$ μs). The spatial distribution of AE events in these two stages was random, without a clear trend of coalescence. As for the unstable crack growth stage, both the number and energy of AE events increased significantly and reached their maximum. The number of AE events initiated per strain change also surged when the axial loading approached the crack damage stress. A clear cluster of AE events can be observed indicating crack coalescence, and the event cluster aligned with the final failure plane of rock samples. The AE results suggested a phased damage evolution of rock samples under triaxial loading, which can assist the characterisation of rock damage initiation.

3.3 Damage Identification and the Evolution of Ultrasonic Wave Velocity

By assuming rock damage and the associated property change are isotropic, a scalar damage parameter was applied in this research. Although the accuracy of isotropic damage assumption is less compared with the two- or four-dimensional damage tensor (Krajcinovic 1996; Murakami and Kamiya 1997), the scalar damage parameter brings unparalleled simplicity in engineering practices and thus it is well accepted by a number of previous studies (Balieu and Kringos 2015; Chen et al. 2015; Miao et al. 2021). According to the equivalent strain theory proposed by Kachanov (1958, 1986, 1992, 1993), damage can be expressed as the reduction of the cross-sectional area of rock material due to microcrack generation. Considering a cylindrical rock sample with a cross-sectional area of A, due to the generation and opening of microcracks and defects, the cross-sectional area of the solid skeleton ($\tilde{A}$) in the sample to sustain load would be less than A. Assuming the area of those defects is A_ω, the effective cross-sectional area can be written as the following equation:

$$\tilde{A} = A - A_\omega \tag{2}$$

The scalar damage variable ω can be defined as the percentage of cross-sectional area reduction:

$$\omega = \frac{A - \tilde{A}}{A} = \frac{A_\omega}{A} \tag{3}$$

The direct measurement of damage is challenging since the internal microcrack evolution is difficult to be measured over the triaxial loading experiments. Therefore, to obtain damage

evolution, Lematitre (1984, 2012) and Lemaitre and Chaboche (1994) proposed the hypothesis of strain equivalence, which states the constitutive equation of the damaged material can be simply represented by replacing the stress with effective stress (stress exerted on rock grains, excluding cracks and voids), as shown in Eq. (4) and Fig. 5:

$$\varepsilon_{ij}^e = \frac{\tilde{\sigma}}{E} = \frac{\sigma}{(1-\omega)E} = \frac{\sigma}{\tilde{E}} \tag{4}$$

where $\tilde{\sigma}$ is effective stress and $\tilde{E}$ is the effective Young's modulus. Both can be used to describe the property of damaged material. To measure damage, the deterioration of the elastic modulus (effective Young's modulus) is normally adopted, namely:

$$C_{ijkl}(\omega) = (1-\omega)C_{ijkl}^0 \tag{5}$$

where $C_{ijkl}(\omega)$ and C_{ijkl}^0 are the fourth-order material stiffness matrix for damaged and undamaged cases. In addition, the P wave velocity can be expressed by the Young's modulus:

$$V_p = \sqrt{\frac{(1-v)E}{(1+v)(1-2v)\rho}} \tag{6}$$

where V_p is P wave velocity. v is Poisson's ratio, which can be considered as a constant during loading due to the isotropic
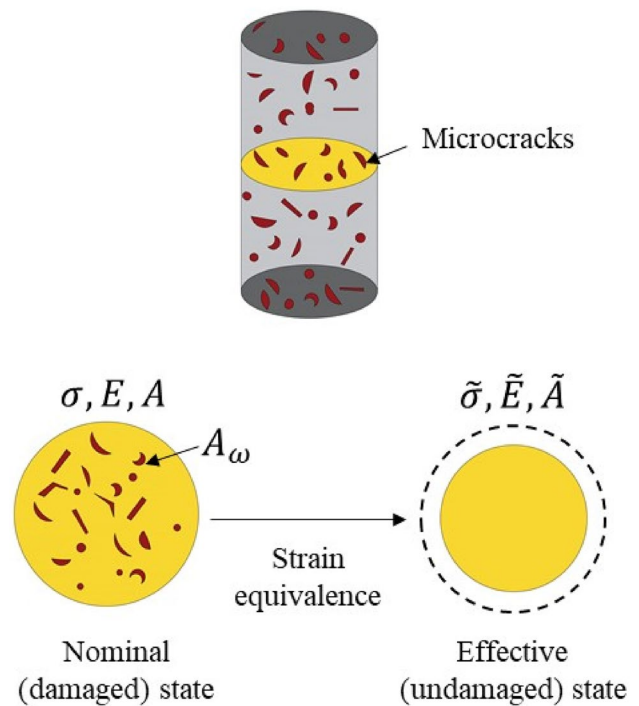

Fig. 5 Scalar damage variable and the hypothesis of strain equivalence (Darabi et al. 2012)

damage assumption. ρ is the density of rock material. Thus, the P wave velocity can become an effective parameter to identify damage evolution inside a rock specimen and its simplicity has already attracted field-scale applications (Zhang et al. 2016).

However, it is not recommended to back calculate Young's modulus directly from the measured P wave velocity using Eq. (6) as a result of potential wave diffusion (Carcione and Picotti 2006). The P wave velocity measurement with low frequency suffers from attenuation in rock micro-grain structure, and therefore, high-frequency P wave with normalization was applied in this research. The application of P wave damage identification on concrete shows that P wave frequency ranging from 0.1 to 1 MHz can be

a reasonable approximation (Berthaud 1988; Lemaitre and Desmorat 2005). Hence, the normalized P wave velocity was used to quantify the damage inside a rock sample, as shown in the following equation (Lemaitre and Desmorat 2005):

$$\omega = 1 - \frac{V_p^2}{V_{p(\max)}^2} \tag{7}$$

where $V_{p(\max)}$ is the maximum P wave velocity and V_p is the P wave velocity measured over triaxial loading.

Figure 6 shows the P wave velocity and volumetric strain evolution of rock samples (since the total rock mass is conserved in the whole test, the density change can be easily calculated by volumetric strain) under different confinement
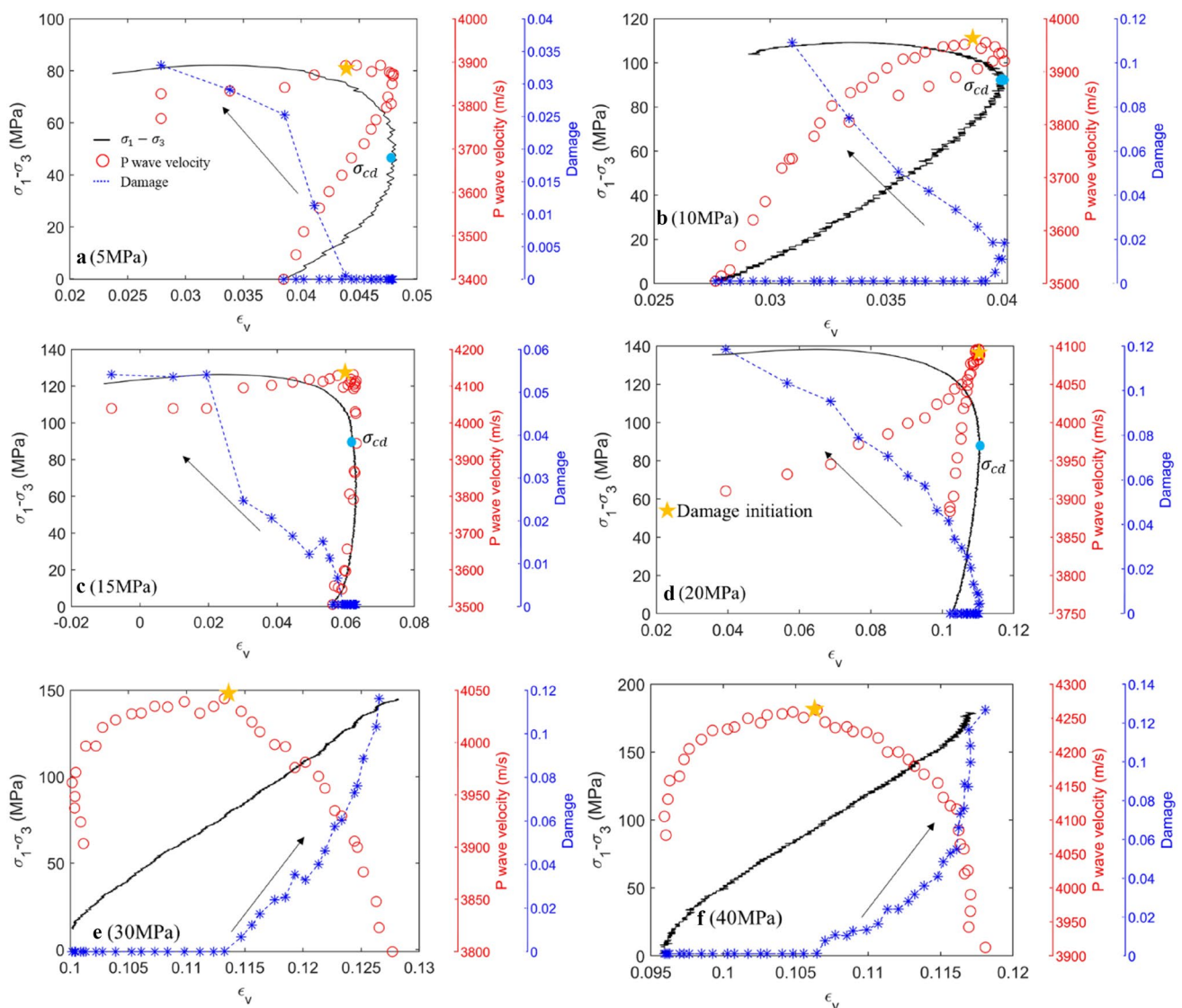

Fig. 6 Evolution of P wave velocity and volumetric strain for triaxial tests on Gosford sandstone under a variety of confinements (5 MPa, 10 MPa, 15 MPa, 20 MPa, 30 MPa and 40 MPa). The crack coales-cence stress (σ_{cd}) is highlighted in low confining stress curves, which can be considered as the damage initiation point

pressures (5 MPa, 10 MPa, 15 MPa, 20 MPa, 30 MPa and 40 MPa). The reduction of P wave velocity can be observed in all six scenarios at around the moment when the axial stress passing σ_{cd}, indicating the generation of microcracking damage in the rock specimen.

Note that we did not observe volumetric strain expansion in the pre-peak stage for 30 MPa and 40 MPa confinement cases and their corresponding P wave velocity drop is less than that in the 10 MPa and 20 MPa confinement cases (same as previous studies Bésuelle et al. 2000; Klein et al. 2001)). This is because the dilation generated by the shearing of microcracks in low confining stress can reduce the P-wave velocity and rock density, whereas high confinement leads to microcrack shearing off.

On the other hand, for the 5 MPa scenario, despite its low confinement, not much damage was recorded in the pre-peak stage due to the strong brittleness of the rock sample, which resulted in the rapid failure of the rock sample with insignificant P wave velocity drop. With the increase of confinement, rock material would typically experience the brittle–ductile transition, yielding more pre-peak damage. Hence, the damage generated in the 10 MPa case is higher than the 5 MPa one.

It is interesting to find that the damage variable ω is closely correlated with the volumetric and lateral strain expansion (dilation), as shown in Fig. 6. As soon as the transition from volumetric compression to dilation occurs, the P wave velocity drops, indicating microcrack-induced damage starts to affect rock mechanical properties (Fig. 6a–d). This phenomenon is also noticed by Ortiz (1985), who defined dilation (ε^+) as the indicator of damage for rock material using the following equation:

$$\varepsilon^+ = \sum_{k=1}^{3} H(\varepsilon_k)\varepsilon_k V^k \otimes V^k \tag{8}$$

where $H(\varepsilon_k)$ is the Heaviside step function for the kth principal strain and V^k is the direction vector of the kth principal strain direction. The start of damage is normally accompanied by the initiation of ε^+ (Shao et al. 2005). Therefore, we proposed that the normalized P wave velocity drop and volumetric strain reversal can be considered as effective parameters to determine the damage evolution of rock materials. The P wave velocity-based damage variable calculated from Eq. (7) would be used as the input parameter for the following elastoplastic damage model.

4 Thermodynamic Framework

4.1 Constitutive Modelling

Based on the analysis of lab test results, this section aims to develop an elastoplastic damage constitutive model under the framework of both the plastic and damage theory for the pre-peak behaviour of rock samples. In the high confinement cases, rock damage was restricted but notable plastic yielding was still generated (see Fig. 2). Therefore, in this model, damage was believed to be affected by the confinement and uncoupled with plastic deformation. A non-associated plastic flow model was adopted that the plastic strain can be induced by both hydrostatic and deviatoric stress in rock samples (considering the effect of confinement). An isotropic P wave velocity-based damage parameter was used to simulate the reduction of rock properties due to microcracking. We also assumed that the whole loading process was isothermal, and the strain increments were infinitesimal. Classically, the total strain can be separated into elastic and plastic components, as shown in the following equation:

$$\varepsilon_{ij} = \varepsilon_{ij}^e + \varepsilon_{ij}^p; d\varepsilon_{ij} = d\varepsilon_{ij}^e + d\varepsilon_{ij}^p \tag{9}$$

where ε_{ij}^e here refers to the elastic strain and ε_{ij}^p indicates the plastic strain. In addition, from a thermodynamics point of view, the reversible energy stored in the rock sample can be expressed by the Helmholtz free energy. A pragmatic approach is to assume that the plastic and damage components of the Helmholtz free energy can be written as two separated parts. This method was also adopted in Rousselier's theory (1981), as explained in Eq. (10) and Fig. 7:

$$\varphi = \varphi_e(\varepsilon_{ij}^e) + \varphi_p(\widetilde{\sigma}_{ij}, \gamma_p) + \varphi_\omega(\varepsilon_{ij}^e, \omega) \tag{10}$$

where γ_p is the plastic hardening variable and ω is the damage variable. Though a few studies proposed that the plastic and damage evolution are fully coupled (Salari et al. 2004; Chen et al. 2010; Wang and Xu 2020), based on the observation in Sect. 3.3, it is suggested that damage and plasticity are not so closely related. As discussed in Fig. 6, less damage is observed under high confinement, while plastic deformation still develops. In addition, previous researchers found that the damage initiation point is prior to or inferior to the plastic initiation point in the loading process (Diederichs et al. 2004; Wang et al. 2016). These results support the argument that the damage evolution and plastic flow can be independent. In addition, in Fig. 7, considering an ideal plastic material with both plasticity (unrecoverable strain) and damage (deterioration in elastic modulus) presence, the Helmholtz free energy is separated into two parts φ_p and φ_ω. In addition, considering the complicated rock engineering environment, the separation of damage and plastic component can largely simplify the model and make it easy for engineering applications. Here, the only difference between the plastic and damage components of Helmholtz free energy is that effective stress ($\widetilde{\sigma}_{ij}$) is used in calculating plastic Helmholtz energy.

Fig. 7 Illustration of the Helmholtz free energy with its elastic (φ_e), plastic (φ_p) and damage (φ_ω) components
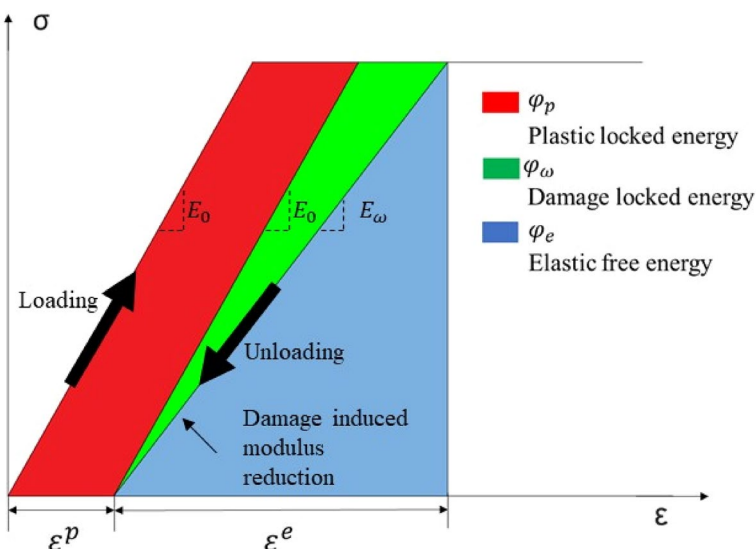
Under the scope of continuum mechanics, the second law of thermodynamics (the Clausius–Duhem inequality) is used to ensure the material is thermodynamically allowable. The Clausius–Duhem inequality indicates the rate of dissipated energy should be positive, as defined in the following equation:

$$\sigma_{ij} : d\varepsilon_{ij} - d\varphi \geq 0 \tag{11}$$

where $d\varphi$ is the total derivative of the Helmholtz free energy, consisting of its partial differential of three independent variables, total strain (ε_{ij}), plastic hardening (γ_p) and damage (ω).

Substituting Eq. (10) into Eq. (11):

$$\left(\sigma_{ij} - \frac{\partial \varphi}{\partial \varepsilon_{ij}}\right) : d\varepsilon_{ij} - \frac{\partial \varphi}{\partial \omega}d\omega - \frac{\partial \varphi}{\partial \gamma_p}d\gamma_p \geq 0 \tag{12}$$

For any strain tensors, the inequality must be satisfied. Therefore, the coefficient before the total strain should be zero and the inequality can be rewritten as Eqs. (13), (14) and (15). Noticing that the damage and plastic strain are unrecoverable from the whole loading process, and therefore, the dispassion from the whole test should be non-negative. Although the P wave measured damage slightly violates the second law proposed here, it is still in an acceptable range and the overall damage evolution trend is consistent with the theoretical equation (see later in Fig. 11):

$$\sigma_{ij} = \frac{\partial \varphi}{\partial \varepsilon_{ij}} \tag{13}$$

$$-\frac{\partial \varphi}{\partial \omega}d\omega \geq 0 \tag{14}$$

$$-\frac{\partial \varphi}{\partial \gamma_p}d\gamma_p \geq 0 \tag{15}$$

For simplicity, the Helmholtz free energy can be written as

$$\varphi = \frac{1}{2}\left(\varepsilon_{ij} - \varepsilon_{ij}^p\right) : C(\omega)_{ijkl} : \left(\varepsilon_{kl} - \varepsilon_{kl}^p\right) + \varphi_p(\widetilde{\sigma}_{ij}, \gamma_p) \tag{16}$$

Therefore, substituting Eq. (16) into Eq. (13):

$$\sigma_{ij} = C(\omega)_{ijkl} : \varepsilon_{kl}^e \tag{17}$$

4.2 Definition of Plastic Evolution

Since one of the major failure modes of rock material is the shear failure, the associated plastic flow may not be applicable to describe the plastic flow of rock shear failure. This is because the direction of plastic strain generated is no longer normal to the plastic yielding surface and the hydrostatic stress can also induce plastic strain. A detailed explanation can be found in Fig. 8.

Therefore, rather than the associated flow rule, the non-associated plastic flow rule was applied in this study, which implies the plastic yielding surface and plastic potential function is no longer coincide with each other. For simplicity, a plastic yielding surface and plastic potential functions were proposed in Eqs. (18) and (19), respectively:

$$f_p(\widetilde{\sigma}_{ij}, \alpha_p) \leq 0 \tag{18}$$

$$g_p(\widetilde{\sigma}_{ij}, \alpha_p) \leq 0 \tag{19}$$

where f_p is the plastic yielding surface (loading surface) and g_p is the plastic potential function. α_p is another plastic hardening variable, which is a conjugated force according

Fig. 8 Typical shear slippage where the associated flow rule is violated. The yielding surface is selected as a cohesionless Mohr–Coulomb criterion. The plastic increment ($d\varepsilon_p$) is no longer perpendicular to the yielding surface (Liu and Zheng 2019)
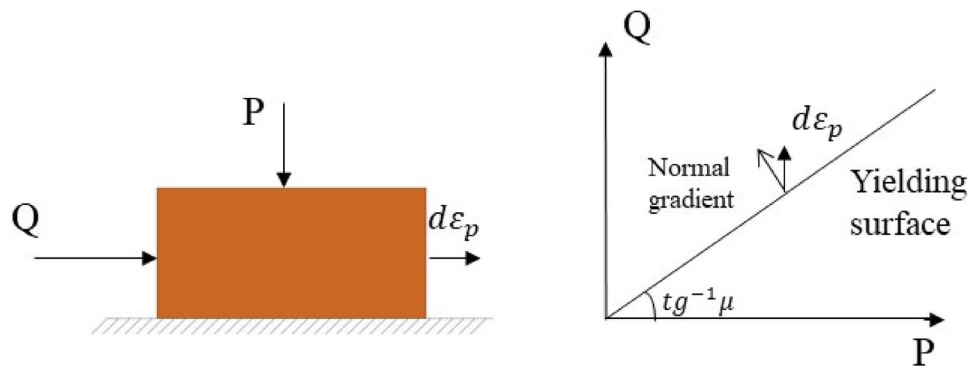
to the plastic hardening variable γ_p, as shown in Eq. (20). α_p controls the hardening (expansion) of the yielding surface:

$$\alpha_p = \frac{\partial \varphi_p}{\partial \gamma_p} \tag{20}$$

The plastic flow rule is, therefore, can be expressed as

$$d\varepsilon_p = d\lambda_p \frac{\partial g_p(\tilde{\sigma}_{ij}, \alpha_p)}{\partial \tilde{\sigma}_{ij}} \tag{21}$$

where λ_p is the plastic multiplier, controlling the magnitude of plastic increment, and $\frac{\partial g_p(\tilde{\sigma}_{ij}, \alpha_p)}{\partial \tilde{\sigma}_{ij}}$ is the gradient of plastic yield potential, which shows the direction of plastic increment. Due to the infinitesimal strain assumption, the consistency law is adopted showing that the plastic increment is small enough. Before and after the plastic increment strain is generated, the stress state is still on the plastic loading surface:

$$df_p = \frac{\partial f_p}{\partial \tilde{\sigma}_{ij}} : d\tilde{\sigma}_{ij} + \frac{\partial f_p}{\partial \alpha_p} d\alpha_p = 0 \tag{22}$$

Substituting Eq. (17) into Eq. (22), we can get that (Shao et al. 2006; Grassl and Jirásek 2006):

$$df_p = \frac{\partial f_p}{\partial \tilde{\sigma}_{ij}} : C^0_{ijkl} : d\varepsilon_{kl} - \frac{\partial f_p}{\partial \tilde{\sigma}_{ij}} : C^0_{ijkl} : d\varepsilon^P_{kl} + \frac{\partial f_p}{\partial \alpha_p} \frac{\partial \alpha_p}{\partial \gamma_p} \frac{\partial \gamma_p}{\partial \varepsilon^P_{ij}} : d\varepsilon^P_{ij} = 0 \tag{23}$$

Substituting Eq. (21) into Eq. (23), the evolution of plastic multiplier can be achieved:

$$d\lambda_p = \frac{\frac{\partial f_p}{\partial \tilde{\sigma}_{ij}} : C^0_{ijkl} : d\varepsilon_{kl}}{\frac{\partial f_p}{\partial \tilde{\sigma}_{ij}} : C^0_{ijkl} : \frac{\partial g_p}{\partial \tilde{\sigma}_{kl}} - \frac{\partial f_p}{\partial \alpha_p} \frac{\partial \alpha_p}{\partial \gamma_p} \left(\frac{\partial \gamma_p}{\partial \varepsilon^P_{ij}} : \frac{\partial g_p}{\partial \tilde{\sigma}_{ij}} \right)} \tag{24}$$

4.3 Definition of Damage Evolution

Similar to the plastic definition, the damage yielding surface and damage potential can be expressed as

$$f_\omega(\varepsilon_{ij}, \omega) \le 0 \tag{25}$$

$$g_\omega(\varepsilon_{ij}, \omega) \le 0 \tag{26}$$

where f_ω is the damage yielding surface (loading surface) and g_ω is the damage potential. ω is the damage variable, which can be written as

$$d\omega = d\lambda_\omega \frac{\partial g_\omega(\varepsilon_{ij}, \omega)}{\partial \varepsilon_{ij}} = d\lambda_\omega \tag{27}$$

where λ_ω is the damage multiplier. Since the damage defined here is a scalar without direction, the gradient of damage potential (g_ω) can be ignored. The damage evolution also obeys the damage consistency law, proposed as

$$df_\omega = \frac{\partial f_\omega}{\partial \varepsilon_{ij}} : d\varepsilon_{ij} + \frac{\partial f_\omega}{\partial \omega} d\omega = 0 \tag{28}$$

Therefore, the evolution of damage multiplier can be expressed as

$$d\lambda_\omega = -\frac{\frac{\partial f_\omega}{\partial \varepsilon_{ij}} : d\varepsilon_{ij}}{\frac{\partial f_\omega}{\partial \omega}} \tag{29}$$

5 Results and Discussion

5.1 Parameters of Plastic Model

To evaluate the plastic strain and plastic multiplier (λ_p) of a rock sample in its plastic deformation stage, the corresponding plastic yielding surface, plastic potential, and hardening

variables are determined in this section. The rock sample is assumed to be isotropic, whose modulus matrix only has two independent variables.

5.1.1 Plastic Yielding Surface (Loading Surface)

Considering the necessary requirements of plastic yielding surface (e.g., pressure sensitivity, non-associated plastic flow, and plastic hardening caused by both hydrostatic and deviatoric stress), based on the results illustrated in Fig. 3, the Drucker–Prager yielding surface was selected, as summarised in the following equations:

$$f_p\left(\tilde{\sigma}_{ij}, \gamma_p, \omega\right) = \alpha \tilde{I}_1 + \sqrt{\tilde{J}_2} - k \tag{30}$$

$$\tilde{I}_1 = \frac{1}{3} tr \tilde{\sigma}_{kk} \tag{31}$$

$$\tilde{J}_2 = \frac{1}{6}\left[2 \times (\tilde{\sigma}_1 - \tilde{\sigma}_3)^2\right] \tag{32}$$

where $\tilde{I}_1$ is the first invariant of effective stress tensor. $\tilde{J}_2$ is the second invariant of effective deviatoric stress tensor. $\tilde{\sigma}_1$ and $\tilde{\sigma}_3$ are the effective axial and lateral stress. k is the D–P parameter to measure the plastic hardening, which controls the expansion of the yielding surface. In this research, all compressive triaxial tests are under monotonic loading, and therefore, only isotropic hardening is considered. Since the Drucker–Prager yielding surface is a symmetrical circle on the π-plane, the effect of Lode's angle on the yielding surface can be ignored.

The plastic hardening variable (γ_p) represents the degree of plastic deformation, and it is also closely related to the plastic component in the Helmholtz free energy (locked energy). The hardening variable selected here is related to the cumulative plastic strain generated in rock samples, as shown in Eq. (33). Under the lab testing condition, the plastic shear strain on the rock surface (rock contact with loading platens) can be ignored since the sample only sustains the loading along the principal stress direction (σ_1 and σ_3), and the plastic stress and strain ought to be coaxial:

$$d\gamma_p = d\varepsilon_i^p = \sqrt{(d\varepsilon_x^p)^2 + (d\varepsilon_y^p)^2 + (d\varepsilon_z^p)^2} \tag{33}$$

$$k = H'(\int d\varepsilon_i^p) \tag{34}$$

where $d\varepsilon_i^p$ is the increment of cumulative plastic strain.

According to the stress–strain curves and AE results presented in Sect. 3, the plastic deformation of rock can be divided into the stable and unstable microcrack generation stages. The plastic strain accelerates with the progress of strain hardening till the shear failure plane is generated. Based on the lab test results, an exponential function was introduced here to represent the relationship between the hardening variable γ_p and k (i.e., the $H'()$ function in Eq. 34). This exponential relationship was also adopted by a few other researchers (Borja et al. 2003; Chiarelli et al. 2003; Salari et al. 2004; Grassl and Jirásek 2006):

$$\gamma_p = \alpha_1 e^{\beta_1 H(k-k_0)} \tag{35}$$

where α_1 and β_1 are two fitting parameters; α_1 determines the magnitude of plastic hardening and β_1 controls the initiation of the unstable plastic evolution stage, $H()$ is the Heaviside step function, introduced in Eq. 8.

5.1.2 Plastic Potential Function

The non-associated plastic flow rule, where the plastic yielding surface and plastic potential function do not coincide, was used in this paper. It was reported that the volumetric strain estimated by the Drucker–Prager criterion in non-associated plastic flow was abnormally higher than the actual test result (Salari et al. 2004). Therefore, a pragmatic and simple assumption in the plastic potential function is to add a correction factor in front of the volumetric component of the Drucker–Prager criterion, which yields:

$$g_p = p\tilde{I}_1 + \sqrt{\tilde{j}_2} \tag{36}$$

where p is the correction factor on the volumetric component of the Drucker–Prager criterion, which is related to the ratio of the hydrostatic plastic strain to deviatoric plastic strain. However, even in the monotonic loading (lab test) condition, the determination of the correction factor is still challenging. With the damage evolution and material hardening, the axial effective stress is changing throughout the whole test, and therefore, the plastic strain ratio is not a constant but a variable depending on the hardening degree. From Eq. (35), the plastic hardening variable γ_p has an exponential correlation with k. Therefore, the volumetric and deviatoric plastic strain should also obey an exponential relation with a clear acceleration at the unstable crack generation stage. The parameter p is related to the ratio between the volumetric and deviatoric plastic strain, which can also be described using an exponential function.

From the test results, the effect of confinement on the volumetric strain was observed, and therefore, it can be deduced that the plastic strain ratio was also related to the confinement, as shown in Fig. 2. In low confinement (5 MPa), rock showed brittle behaviour, and therefore, the volumetric plastic strain was subtle during the whole pre-peak stage, while for high confinement (30 MPa and 40 MPa scenarios), the lateral expansion (dilation) was constrained, because new

asperities were sheared off. Therefore, the p ratio between volumetric and deviatoric plastic strain should first undergo an increase and then decrease to nearly zero, according to our lab observation. Based on Sect. 3.3, the maximum volumetric strain expansion was initiated at around 20 MPa confinement and ceased when 30 MPa confinement was applied. Inspired by previous studies (Bao et al. 2013; Ding and Zhang 2017), we used a quadratic function to express the relationship between the confinement and the plastic hardening variable:

$$p\left(\gamma_p, \tilde{\sigma}_3\right) = (\alpha_2(\tilde{\sigma}_3 - \sigma_\alpha)^2 + \Upsilon_2)e^{\beta_2\gamma_p} \tag{37}$$

where α_2, β_2 and Υ_2 are the fitting parameter to control the magnitude of p. These parameters can be considered as a measurement of rock properties from brittleness to ductility. σ_α is the critical confinement, indicating the confinement stress, where the volumetric expansion is the highest, which was found at 20 MPa based on lab observations.

5.2 Plastic Model Fitted by Rock Triaxial Test Results

There are two relations that need to be fit by experiment results, i.e., the plastic hardening Eq. (35) and plastic potential Eq. (37). To obtain the best fitting parameters for the elastoplastic constitutive model, MATLAB curve fitting toolbox was used to fit these equations. The fitting method is the well-accepted nonlinear least square method. The optimization algorithm is the Trust-Region algorithm, where a region is defined around the best solution. Then the Trust-Region algorithm uses a defined model (e.g., quadratic functions in this research) to approach the target function, ensuring the best convergence of fitting results. Then, those two relations can be fitted accordingly.

Using the parameters summarised in Table 1, the mechanical response of rock material under triaxial loading can be obtained. The axial and circumferential loading behaviour are presented in Figs. 9 and 10, respectively. Comparing the theoretical model with the lab test results, a good consistency can be observed at all six different confinements. Since the post-peak stage can be highly affected by the

Table 1 Fitting parameters used in the plastic evolution of the pre-peak stage

Strength parameter	$\alpha = -0.2341$	$k_0 = 19.96$ MPa	$k_f = 37.1$ MPa
Plastic hardening	$\alpha_1 = 0.004452$	$\beta_1 = 0.1246$	
Plastic potential	$\alpha_2 = -0.001435$	$\beta_2 = 15.28$ $\Upsilon_2 = 0.8889$	
Critical confinement	$\sigma_\alpha = 20$ MPa		

randomness of rock fracture initiation, where a stress drop and lateral expansion can suddenly occur violating the continuity hypothesis in the continuum mechanics, the theoretical model was only applied to the pre-peak stage. In addition, the failure plane generated in the post-failure stage shows strong anisotropy and heterogeneity, and therefore, the scalar damage variable is no more applicable in that case. Further study is still required to implement the elastoplastic damage model in the post-peak stage.

5.3 Damage Model Fitted by Rock Triaxial Test Results

In previous sections, the plastic evolution law is discussed in detail. The damage evolution is similar to the plastic counterpart, but with its own hardening parameter and yielding surface. To explain the damage evolution, from the thermodynamic point of view, the damage energy release rate Y (conjugate force of damage variable) can be expressed as

$$Y_{ij} = -\frac{\partial \varphi}{\partial \omega} = \frac{1}{2}\left(\varepsilon_{ij} - \varepsilon_{ij}^p\right) : C_{ijkl}^0 : \left(\varepsilon_{ij} - \varepsilon_{ij}^p\right) \tag{38}$$

Since the scalar damage variable is assumed, the damage potential surface can be ignored. The damage identification can be separated into two subsequence questions, namely, how does damage initiate and how does it propagate. Inspired by previous studies, we proposed the damage initiation energy release rate is proportional to the confinement, as shown in Fig. 11a. From Fig. 6, damage accelerates as the sample approaches its peak stress. Hence, an exponential function was often used to describe the damage yielding surface and its hardening variable, which is also adopted by a few studies (Rinaldi et al. 2007; Cao et al. 2010; Chen et al. 2015). The damage yielding surface is defined as

$$f_\omega = \alpha_\omega \sigma_3 \times \log(b_\omega \times H(Y - Y_0) + 1) \tag{39}$$

where a_ω and b_ω are fitting parameters to control the initiation of damage and the damage evolution rate. Apparently, the whole damage process was strongly related to the confinement of specimens in these tests, as illustrated in Fig. 6. Hence, σ_3 was used to reflect the effect of confinement on the damage yielding surface. Note that for the 5 MPa confinement scenario, owing to great brittleness, the damage evolution is not sufficient (less than 2%), and therefore, we do not interpret this group of data. The fitting parameters based on test results are listed in Table 2. The damage evolution can be modelled by these parameters, as shown in Fig. 11.

A high agreement can be observed between the model results and the test damage results calculated based on Eq. (7). Since all the data analysed here are for the pre-peak stage, this observation shows that damage can be induced even before the structural failure of a rock specimen.
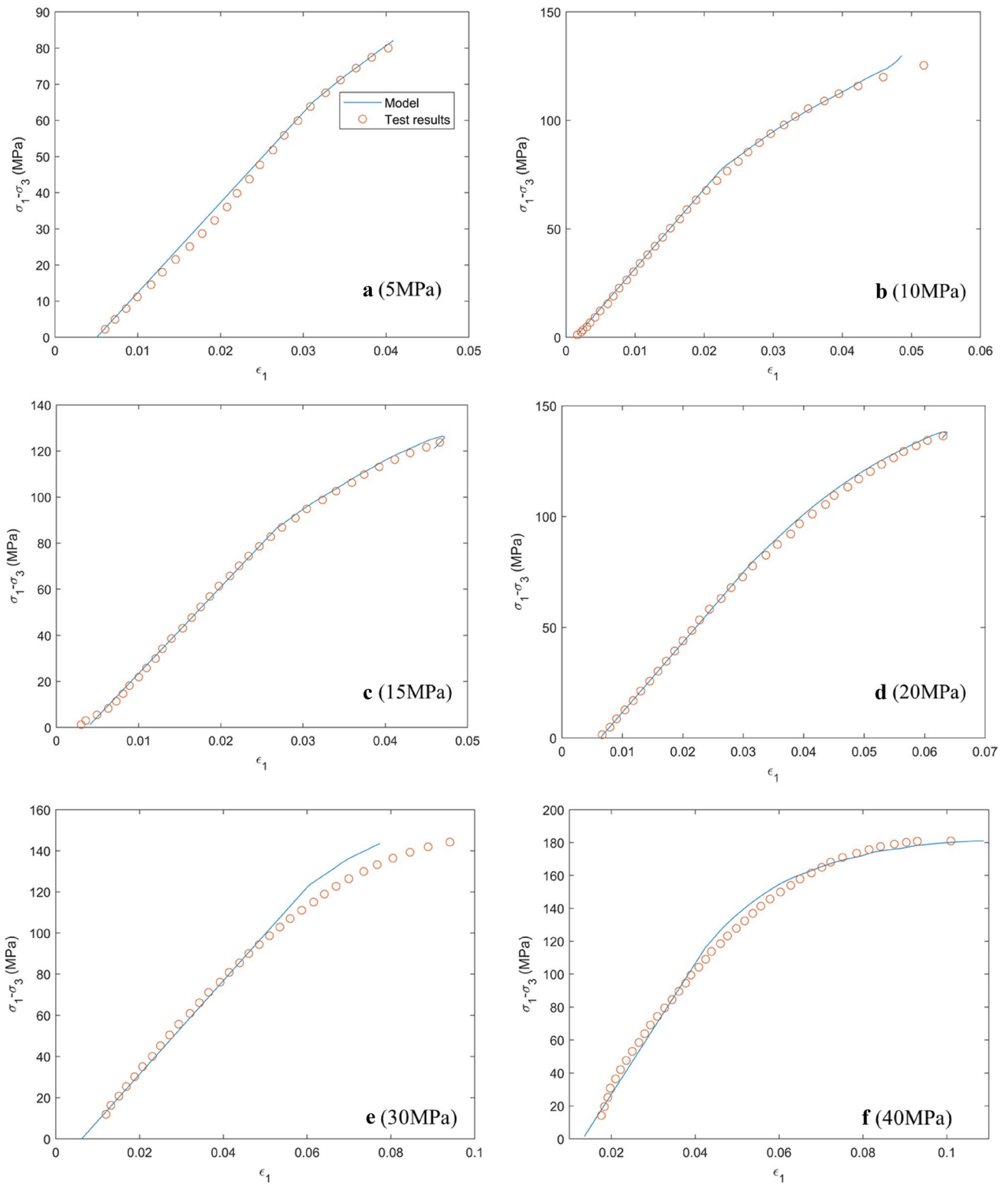
Fig. 9 Comparison of model results and lab test data in the axial direction under various confinements (5 MPa, 10 MPa, 15 MPa, 20 MPa, 30 MPa and 40 MPa)
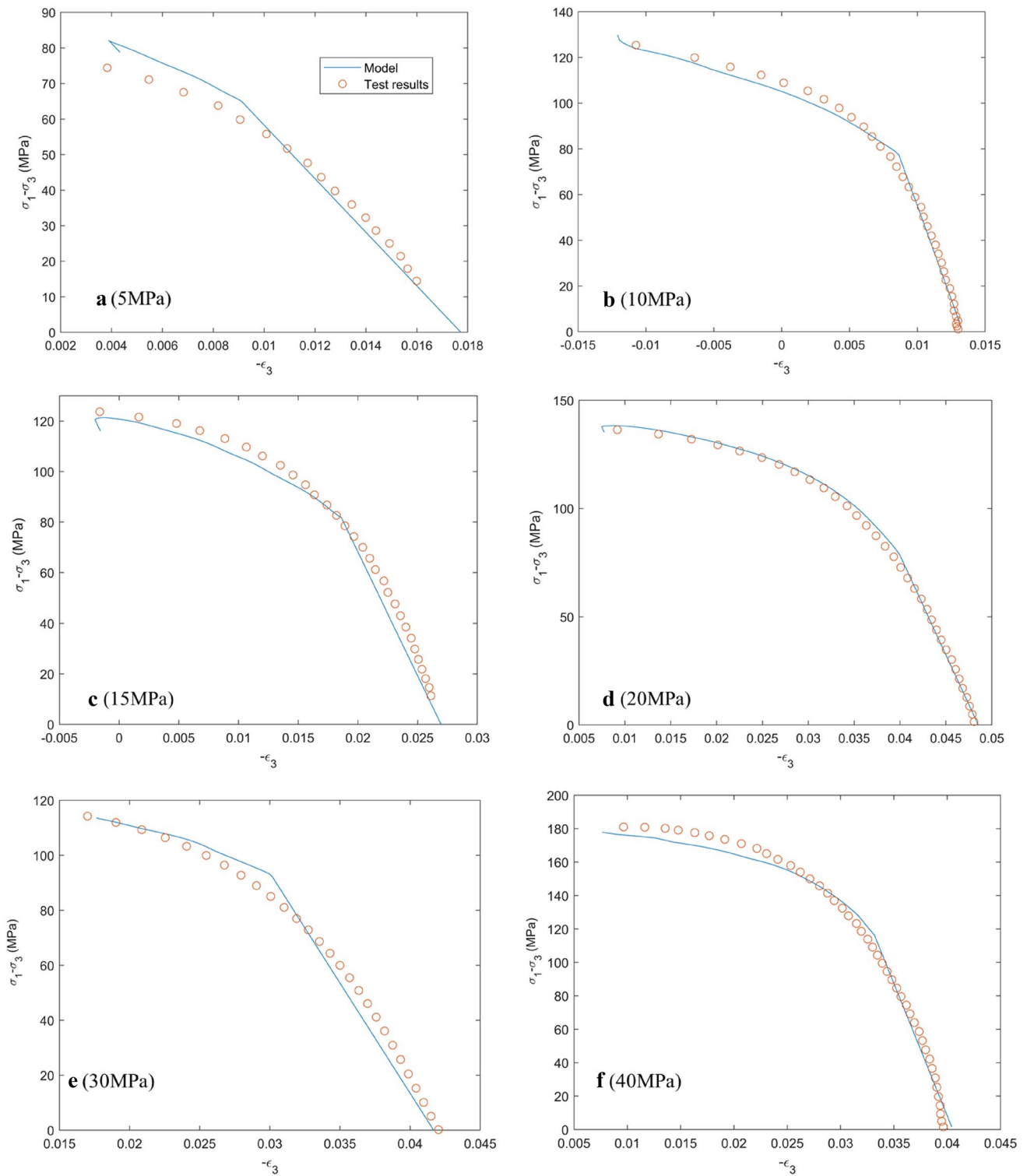
Fig. 10 Comparison of model results and lab test data in the circumferential direction under various confinements (5 MPa, 10 MPa, 15 MPa, 20 MPa, 30 MPa and 40 MPa)
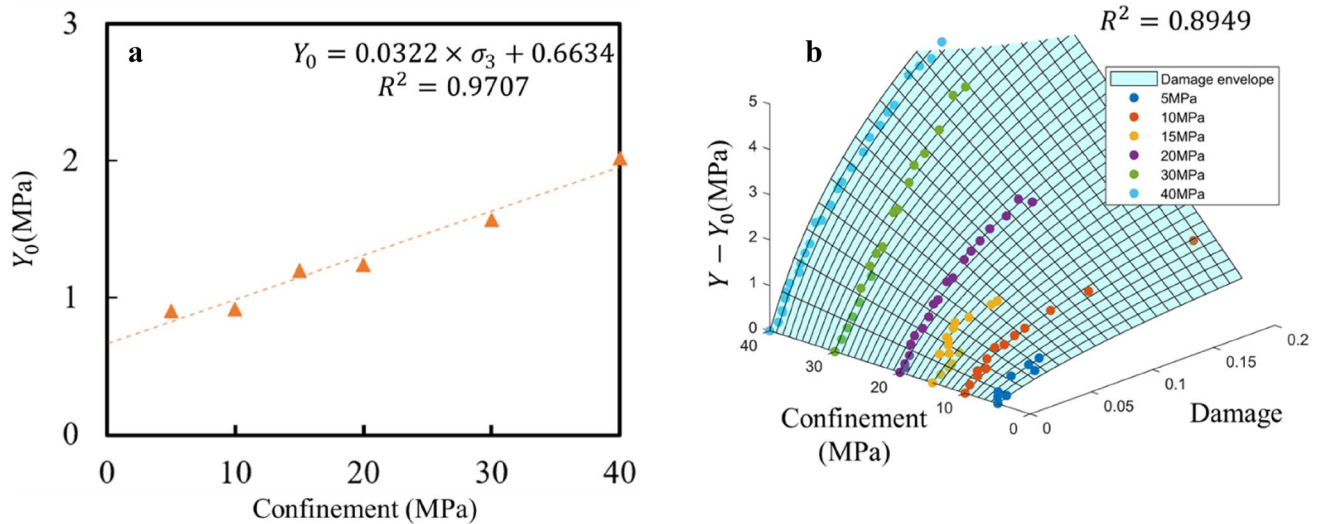
Fig. 11 Comparison of model and lab test results of damage behaviour under various confinements (10 MPa, 15 MPa, 20 MPa, 30 MPa, 40 MPa)

Table 2 Fitting parameters used in the damage evolution

a_ω	b_ω
0.0964	22.01

Interestingly, we found that damage can be restricted by high confinement (Fig. 11), where the ultimate damage drops from 0.16 at 20 MPa to only around 0.1 and 0.12 at 30 MPa and 40 MPa confinement.

6 Conclusions and Future Work

A new elastoplastic damage model has been proposed to describe the pre-peak deformation of Gosford sandstone with the assistance of two NDT methods (AE and ultrasonic wave velocity measurement). The precise damage variable is back-calculated from the ultrasonic wave velocity measurement in the loading cycle. Non-associated plastic flow is applied to control the direction of plastic increment. In addition, damage evolution is related to its conjugate variable according to the Helmholtz free energy, namely the damage energy release rate Y. The main findings can be summarised as follows:

1. The lab test results show that loading-induced rock damage can be well reflected by the drop in ultrasonic wave velocity. In addition, different loading stages (stable crack initiation and unstable crack initiation) are identified by the stress–strain curves, AE data and ultrasonic wave velocity change.

2. The damage evolution depends on its conjugate force Y, referring to damage energy release rate. An exponential relationship was proposed to depict the acceleration of damage while approaching the peak stress.

3. The proposed model shows relatively consistent results with the lab measurements, enabling it to capture main rock deformation characteristics during triaxial loading. Since the model was based on the D–P criterion, its application in other numerical software packages will be relatively easy. In addition, P wave velocity is an input parameter required in this model, which is relatively easy to obtain by active ultrasonic wave velocity measurement or passive AE tomography in the field. In future work, the proposed model will be programmed to numerically reproduce rock lab testing results and upscaled for engineering field applications.

Declarations

References

Attewell PB, Farmer IW (1973) Fatigue behaviour of rock. Int J Rock Mech Min Sci Geomech Abst 10:1–9. https://doi.org/10.1016/0148-9062(73)90055-7

Balieu R, Kringos N (2015) A new thermodynamical framework for finite strain multiplicative elastoplasticity coupled to anisotropic damage. Int J Plast 70:126–150. https://doi.org/10.1016/j.ijplas.2015.03.006

Bao JQ, Long X, Tan KH, Lee CK (2013) A new generalized Drucker–Prager flow rule for concrete under compression. Eng Struct 56:2076–2082. https://doi.org/10.1016/j.engstruct.2013.08.025

Berthaud Y (1988) Mesure de l'endommagement du béton par une méthode ultrasonore. PhD Thesis, Paris 6

Bésuelle P, Desrues J, Raynaud S (2000) Experimental characterisation of the localisation phenomenon inside a Vosges sandstone in a triaxial cell. Int J Rock Mech Min Sci 37:1223–1237. https://doi.org/10.1016/S1365-1609(00)00057-5

Borja RI, Sama KM, Sanz PF (2003) On the numerical integration of three-invariant elastoplastic constitutive models. Comput Methods Appl Mech Eng 192:1227–1258

Brace WF, Paulding BW Jr, Scholz CH (1966) Dilatancy in the fracture of crystalline rocks. J Geophys Res 71:3939–3953

Cai M, Kaiser PK, Tasaka Y, Maejima T, Morioka H, Minami M (2004) Generalized crack initiation and crack damage stress thresholds of brittle rock masses near underground excavations. Int J Rock Mech Min Sci 41:833–847. https://doi.org/10.1016/j.ijrmms.2004.02.001

Cai W, Dou L, Ju Y, Cao W, Yuan S, Si G (2018) A plastic strain-based damage model for heterogeneous coal using cohesion and dilation angle. Int J Rock Mech Min Sci 110:151–160. https://doi.org/10.1016/j.ijrmms.2018.08.001

Cai W, Dou L, Si G, Cao A, Gong S, Wang G, Yuan S (2019) A new seismic-based strain energy methodology for coal burst forecasting in underground coal mines. Int J Rock Mech Min Sci 123:104086. https://doi.org/10.1016/j.ijrmms.2019.104086

Cao WG, Zhao H, Li X, Zhang YJ (2010) Statistical damage model with strain softening and hardening for rocks under the influence of voids and volume changes. Can Geotech J 47:857–871. https://doi.org/10.1139/T09-148

Cao W, Shi JQ, Durucan S, Si G, Korre A (2020) Gas-driven rapid fracture propagation under unloading conditions in coal and gas outbursts. Int J Rock Mech Min Sci 130:104325. https://doi.org/10.1016/j.ijrmms.2020.104325

Carcione JM, Picotti S (2006) P-wave seismic attenuation by slow-wave diffusion: effects of inhomogeneous rock properties. Geophysics 71:O1–O8

Chen L, Shao JF, Huang HW (2010) Coupled elastoplastic damage modeling of anisotropic rocks. Comput Geotech 37:187–194. https://doi.org/10.1016/j.compgeo.2009.09.001

Chen L, Wang C, Liu J, Liu J, Wang J, Jia Y, Shao J (2015) Damage and plastic deformation modeling of Beishan granite under compressive stress conditions. Rock Mech Rock Eng 48:1623–1633. https://doi.org/10.1007/s00603-014-0650-5

Chen S, Qiao C, Ye Q, Khan MU (2018) Comparative study on three-dimensional statistical damage constitutive modified model of rock based on power function and Weibull distribution. Environ Earth Sci 77:108. https://doi.org/10.1007/s12665-018-7297-6

Chiarelli AS, Shao J, Hoteit N (2003) Modeling of elastoplastic damage behavior of a claystone. Int J Plast 19:23–45. https://doi.org/10.1016/S0749-6419(01)00017-1

Darabi MK, Al-Rub RKA, Little DN (2012) A continuum damage mechanics framework for modeling micro-damage healing. Int J Solids Struct 49:492–513

Diederichs MS, Kaiser PK, Eberhardt E (2004) Damage initiation and propagation in hard rock during tunnelling and the influence of near-face stress rotation. Int J Rock Mech Min Sci 41:785–812. https://doi.org/10.1016/j.ijrmms.2004.02.003

Ding X, Zhang G (2017) Coefficient of equivalent plastic strain based on the associated flow of the Drucker–Prager criterion. Int J Non Linear Mech 93:15–20. https://doi.org/10.1016/j.ijnonlinmec.2017.04.018

Fairhurst CE, Hudson JA (1999) Draft ISRM suggested method for the complete stress-strain curve for intact rock in uniaxial compression. Int J Rock Mech Min Sci 36:279–289

Fathi A, Moradian Z, Rivard P, Ballivy G (2016) Shear mechanism of rock joints under pre-peak cyclic loading condition. Int J Rock Mech Min Sci 83:197–210

Ganne P, Vervoort A, Wevers M (2007) Quantification of pre-peak brittle damage: correlation between acoustic emission and observed micro-fracturing. Int J Rock Mech Min Sci 44:720–729

Grassl P, Jirásek M (2006) Damage-plastic model for concrete failure. Int J Solids Struct 43:7166–7196. https://doi.org/10.1016/j.ijsolstr.2006.06.032

Hill R (1948) A theory of the yielding and plastic flow of anisotropic metals. Proc R Soc Lond A 193:281–297

Homand F, Hoxha D, Belem T et al (2000) Geometric analysis of damaged microcracking in granites. Mech Mater 32:361–376. https://doi.org/10.1016/S0167-6636(00)00005-3

Ishida T, Labuz JF, Manthei G et al (2017) ISRM suggested method for laboratory acoustic emission monitoring. Rock Mech Rock Eng 50:665–674

Iyare UC, Blake OO, Ramsook R (2021) Estimating the uniaxial compressive strength of argillites using Brazilian tensile strength, ultrasonic wave velocities, and elastic properties. Rock Mech Rock Eng 54:2067–2078. https://doi.org/10.1007/s00603-020-02358-y

Kachanov LM (1958) Time of the rupture process under creep conditions. Izvestiia Akademii Nauk SSSR, Otdelenie Teckhnicheskikh Nauk 8:26–31

Kachanov L (1986) Introduction to continuum damage mechanics. Springer

Kachanov M (1992) Effective elastic properties of cracked solids: critical review of some basic concepts. Appl Mech Rev 45:304–335. https://doi.org/10.1115/1.3119761

Kachanov M (1993) Elastic Solids with many cracks and related problems. In: Hutchinson JW, Wu TY (eds) Advances in applied mechanics. Elsevier, pp 259–445

Keneti A, Pouragha M, Sainsbury B-A (2021) Review of design parameters for discontinuous numerical modelling of excavations in the Hawkesbury Sandstone. Eng Geol 288:106158. https://doi.org/10.1016/j.enggeo.2021.106158

Klein E, Baud P, Reuschlé T, Wong T (2001) Mechanical behaviour and failure mode of bentheim sandstone under triaxial compression. Phys Chem Earth Part A 26:21–25. https://doi.org/10.1016/S1464-1895(01)00017-5

Kong R, Feng XT, Zhang X, Yang C (2018) Study on crack initiation and damage stress in sandstone under true triaxial compression. Int J Rock Mech Min Sci 106:117–123. https://doi.org/10.1016/j.ijrmms.2018.04.019

Krajcinovic D (1996) Damage mechanics. Elsevier, North Holland, Amsterdam

Lemaitre J (1984) How to use damage mechanics. Nucl Eng Des 80:233–245. https://doi.org/10.1016/0029-5493(84)90169-9

Lemaitre J (2012) A course on damage mechanics. Springer

Lemaitre J, Chaboche J-L (1994) Mechanics of solid materials. Cambridge University Press

Lemaitre J, Desmorat R (eds) (2005) Background on continuum damage mechanics. In: Engineering Damage Mechanics: Ductile, Creep, Fatigue and Brittle Failures. Springer, Berlin, Heidelberg, pp 1–76

Lemaitre J, Desmorat R, Sauzay M (2000) Anisotropic damage law of evolution. Eur J Mech A Solids 19:187–208. https://doi.org/10.1016/S0997-7538(00)00161-3

Li J, Chen J (2009) Stochastic dynamics of structures. Wiley

Li J, Yan Q, Chen JB (2012) Stochastic modeling of engineering dynamic excitations for stochastic dynamics of structures. Probab Eng Mech 27:19–28

Li L, Hagan PC, Saydam S et al (2016a) Parametric study of rockbolt shear behaviour by double shear test. Rock Mech Rock Eng 49:4787–4797

Li L, Hagan PC, Saydam S, Hebblewhite B (2016b) Shear resistance contribution of support systems in double shear test. Tunn Undergr Space Technol 56:168–175. https://doi.org/10.1016/j.tust.2016.03.011

Li Y, Oh J, Mitra R, Canbulat I (2017) A fractal model for the shear behaviour of large-scale opened rock joints. Rock Mech Rock Eng 50:67–79

Li B, Lan J, Si G, Lin G, Hu L (2020a) NMR-based damage characterisation of backfill material in host rock under dynamic loading. Int J Min Sci Technol 30(3):329–335. https://doi.org/10.1016/j.ijmst.2020.03.015

Li T, Pei X, Guo J et al (2020b) An energy-based fatigue damage model for sandstone subjected to cyclic loading. Rock Mech Rock Eng 53:5069–5079. https://doi.org/10.1007/s00603-020-02209-w

Li Z, Liu D, Cai Y, Wang Y, Si G (2020c) Evaluation of coal petrophysics incorporating fractal characteristics by mercury intrusion porosimetry and low-field NMR. Fuel 263:116802. https://doi.org/10.1016/j.fuel.2019.116802

Li X, Chen S, Wang E, Li Z (2021) Rockburst mechanism in coal rock with structural surface and the microseismic (MS) and electromagnetic radiation (EMR) response. Eng Fail Anal 124:105396. https://doi.org/10.1016/j.engfailanal.2021.105396

Liu Y, Zheng Y (2019) Plastic mechanics of geomaterial. Springer

Liu XR, Kou MM, Lu YM, Liu YQ (2018) An experimental investigation on the shear mechanism of fatigue damage in rock joints under pre-peak cyclic loading condition. Int J Fatigue 106:175–184. https://doi.org/10.1016/j.ijfatigue.2017.10.007

Lockner DA, Moore DE, Reches Z (1992) Microcrack interaction leading to shear fracture. OnePetro

Lv A, Masoumi H, Walsh SDC, Roshan H (2019) Elastic-softening-plasticity around a borehole: an analytical and experimental study. Rock Mech Rock Eng 52:1149–1164. https://doi.org/10.1007/s00603-018-1650-7

Martin CD, Chandler NA (1994) The progressive fracture of Lac du Bonnet granite. In: International journal of rock mechanics and mining sciences and geomechanics abstracts. Elsevier, pp 643–659

Masoumi H, Saydam S, Hagan PC (2016) Unified size-effect law for intact rock. Int J Geomech 16:04015059. https://doi.org/10.1061/(ASCE)GM.1943-5622.0000543

Masoumi H, Horne J, Timms W (2017) Establishing empirical relationships for the effects of water content on the mechanical behavior of gosford sandstone. Rock Mech Rock Eng 50:2235–2242. https://doi.org/10.1007/s00603-017-1243-x

Miao S, Pan PZ, Zhao X et al (2021) Experimental study on damage and fracture characteristics of beishan granite subjected to high-temperature treatment with DIC and AE techniques. Rock Mech Rock Eng 54:721–743. https://doi.org/10.1007/s00603-020-02271-4

Munoz H, Taheri A, Chanda EK (2016) Fracture energy-based brittleness index development and brittleness quantification by pre-peak strength parameters in rock uniaxial compression. Rock Mech Rock Eng 49:4587–4606

Murakami S, Kamiya K (1997) Constitutive and damage evolution equations of elastic-brittle materials based on irreversible thermodynamics. Int J Mech Sci 39:473–486. https://doi.org/10.1016/S0020-7403(97)87627-8

Nicksiar M, Martin CD (2012) Evaluation of methods for determining crack initiation in compression tests on low-porosity rocks. Rock Mech Rock Eng 45:607–617

Oh J, Li Y, Mitra R, Canbulat I (2017) A numerical study on dilation of a saw-toothed rock joint under direct shear. Rock Mech Rock Eng 50:913–925

Ord A, Vardoulakis I, Kajewski R (1991) Shear band formation in Gosford Sandstone. Int J Rock Mech Min Sci Geomech Abstr 28:397–409. https://doi.org/10.1016/0148-9062(91)90078-Z

Ortiz M (1985) A constitutive theory for the inelastic behavior of concrete. Mech Mater 4:67–93

Patton FD (1966) Multiple modes of shear failure. In: Rock. OnePetro

Qin Q, Bassani JL (1992) Non-associated plastic flow in single crystals. J Mech Phys Solids 40:835–862. https://doi.org/10.1016/0022-5096(92)90006-N

Raniecki B, Bruhns OT (1981) Bounds to bifurcation stresses in solids with non-associated plastic flow law at finite strain. J Mech Phys Solids 29:153–172. https://doi.org/10.1016/0022-5096(81)90021-1

Rinaldi A, Krajcinovic D, Mastilovic S (2007) Statistical damage mechanics and extreme value theory. Int J Damage Mech 16:57–76

Roshan H, Sari M, Arandiyan H et al (2016) Total porosity of tight rocks: a welcome to the heat transfer technique. Energy Fuels 30:10072–10079

Roshan H, Masoumi H, Regenauer-Lieb K (2017) Frictional behaviour of sandstone: a sample-size dependent triaxial investigation. J Struct Geol 94:154–165

Rousselier G (1981) Finite deformation constitutive relations including ductile fracture damage. Three-Dimensional Constitutive Relations and Ductile Fracture Edition North-Holland Publ Comp 331–355

Salari MR, Saeb SA, Willam KJ et al (2004) A coupled elastoplastic damage model for geomaterials. Comput Methods Appl Mech Eng 193:2625–2643

Shao JF, Ata N, Ozanam O (2005) Study of desaturation and resaturation in brittle rock with anisotropic damage. Eng Geol 81:341–352. https://doi.org/10.1016/j.enggeo.2005.06.015

Shao JF, Jia Y, Kondo D, Chiarelli AS (2006) A coupled elastoplastic damage model for semi-brittle materials and extension to unsaturated conditions. Mech Mater 38:218–232

Shen P, Tang H, Ning Y, Xia D (2019) A damage mechanics based on the constitutive model for strain-softening rocks. Eng Fract Mech 216:106521. https://doi.org/10.1016/j.engfracmech.2019.106521

Shojaei A, Dahi Taleghani A, Li G (2014) A continuum damage failure model for hydraulic fracturing of porous rocks. Int J Plast 59:199–212. https://doi.org/10.1016/j.ijplas.2014.03.003

Si G, Durucan S, Jamnikar S, Lazar J, Abraham K, Korre A, Shi JQ, Zavšek S, Mutke G, Lurka A (2015) Seismic monitoring and analysis of excessive gas emissions in heterogeneous coal seams. Int J Coal Geol 149:41–54. https://doi.org/10.1016/j.coal.2015.06.016

Si G, Cai W, Wang S, Li X (2020) Prediction of relatively high-energy seismic events using spatial-temporal parametrisation of mining-induced seismicity. Rock Mech Rock Eng 53:5111–5132. https://doi.org/10.1007/s00603-020-02210-3

Singh SK (1988) Relationship among fatigue strength, mean grain size and compressive strength of a rock. Rock Mech Rock Eng 21:271–276. https://doi.org/10.1007/BF01020280

Su G, Shi Y, Feng X et al (2018) True-triaxial experimental study of the evolutionary features of the acoustic emissions and sounds of rockburst processes. Rock Mech Rock Eng 51:375–389. https://doi.org/10.1007/s00603-017-1344-6

Tang CA, Chen ZH, Xu XH, Li C (1997) A theoretical model for kaiser effect in rock. Pure Appl Geophys 150:203–215. https://doi.org/10.1007/s000240050073

Vásárhelyi B, Bobet A (2000) Modeling of crack initiation, propagation and coalescence in uniaxial compression. Rock Mech Rock Eng 33:119–139. https://doi.org/10.1007/s006030050038

Wang S, Xu W (2020) A coupled elastoplastic anisotropic damage model for rock materials. Int J Damage Mech 29:1222–1245. https://doi.org/10.1177/1056789520904093

Wang HL, Xu WY, Jia CJ et al (2016) Experimental research on permeability evolution with microcrack development in sandstone under different fluid pressures. J Geotech Geoenviron Eng 142:04016014. https://doi.org/10.1061/(ASCE)GT.1943-5606.0001462

Wilkins ML (1963) Calculation of elastic-plastic flow. California Univ Livermore Radiation Lab

Wu B, Yao W, Xia K (2016) An experimental study of dynamic tensile failure of rocks subjected to hydrostatic confinement. Rock Mech Rock Eng 49:3855–3864. https://doi.org/10.1007/s00603-016-0946-8

Xu C, Lin C, Kang Y, You L (2018) An experimental study on porosity and permeability stress-sensitive behavior of sandstone under hydrostatic compression: characteristics, mechanisms and controlling factors. Rock Mech Rock Eng 51:2321–2338. https://doi.org/10.1007/s00603-018-1481-6

Xu J, Haque A, Gong W et al (2020) Experimental study on the bearing mechanisms of rock-socketed piles in soft rock based on micro X-ray CT analysis. Rock Mech Rock Eng 53:3395–3416. https://doi.org/10.1007/s00603-020-02121-3

Zhang ZH, Tang CA (2020) A novel method for determining the crack closure stress of brittle rocks subjected to compression. Rock Mech Rock Eng 53:4279–4287. https://doi.org/10.1007/s00603-020-02156-6

Zhang JC, Xu WY, Wang HL et al (2016) A coupled elastoplastic damage model for brittle rocks and its application in modelling underground excavation. Int J Rock Mech Min Sci 84:130–141. https://doi.org/10.1016/j.ijrmms.2015.11.011

Zhang J, Lin Z, Dong B, Guo R (2021a) Triaxial compression testing at constant and reducing confining pressure for the mechanical characterization of a specific type of sandstone. Rock Mech Rock Eng 54:1999–2012. https://doi.org/10.1007/s00603-020-02357-z

Zhang XP, Lv GG, Liu QS et al (2021b) Identifying accurate crack initiation and propagation thresholds in siliceous siltstone and limestone. Rock Mech Rock Eng 54:973–980. https://doi.org/10.1007/s00603-020-02277-y

Zhang Y, Feng X-T, Yang C et al (2021c) Evaluation method of rock brittleness under true triaxial stress states based on pre-peak deformation characteristic and post-peak energy evolution. Rock Mech Rock Eng 54:1277–1291. https://doi.org/10.1007/s00603-020-02330-w

Zhao Y (1998) Crack pattern evolution and a fractal damage constitutive model for rock. Int J Rock Mech Min Sci 35:349–366. https://doi.org/10.1016/S0148-9062(97)00340-9

Zhao XG, Cai M, Wang J et al (2015) Objective determination of crack initiation stress of brittle rocks under compression using AE measurement. Rock Mech Rock Eng 48:2473–2484

Zhao Y, Yang T, Zhang P et al (2017) The analysis of rock damage process based on the microseismic monitoring and numerical simulations. Tunn Undergr Space Technol 69:1–17. https://doi.org/10.1016/j.tust.2017.06.002

Publisher's Note Springer Nature remains neutral with regard to jurisdictional claims in published maps and institutional affiliations.